materials

MDPI

Article

A p–n Junction by Coupling Amine-Enriched Brookite–TiO_2 Nanorods with Cu_xS Nanoparticles for Improved Photocatalytic CO_2 Reduction

Zhangjing Chen [1], Xueteng Zhu [1], Jinyan Xiong [2,*], Zhipan Wen [3] and Gang Cheng [1,*]

[1] School of Chemistry and Environmental Engineering, Wuhan Institute of Technology, Donghu New & High Technology Development Zone, Wuhan 430205, China
[2] College of Chemistry and Chemical Engineering, Wuhan Textile University, Wuhan 430200, China
[3] State Key Laboratory of New Textile Materials and Advanced Processing Technologies, Wuhan Textile University, Wuhan 430200, China
* Correspondence: xjybear@163.com (J.X.); gchenglab@163.com (G.C.)

Abstract: Photocatalytic CO_2 reduction is a promising technology for reaching the aim of "carbon peaking and carbon neutrality", and it is crucial to design efficient photocatalysts with a rational surface and interface tailoring. Considering that amine modification on the surface of the photocatalyst could offer a favorable impact on the adsorption and activation of CO_2, in this work, amine-modified brookite TiO_2 nanorods (NH_2-B-TiO_2) coupled with Cu_xS (NH_2-B-TiO_2-Cu_xS) were effectively fabricated via a facile refluxing method. The formation of a p–n junction at the interface between the NH_2-B-TiO_2 and the Cu_xS could facilitate the separation and transfer of photogenerated carriers. Consequently, under light irradiation for 4 h, when the Cu_xS content is 16%, the maximum performance for conversion of CO_2 to CH_4 reaches at a rate of 3.34 μmol g^{-1} h^{-1} in the NH_2-B-TiO_2-Cu_xS composite, which is approximately 4 times greater than that of pure NH_2-B-TiO_2. It is hoped that this work could deliver an approach to construct an amine-enriched p–n junction for efficient CO_2 photoreduction.

Keywords: amine modification; charge separation; p–n junction; photocatalytic CO_2 reduction; TiO_2-Cu_xS composites

check for updates

Citation: Chen, Z.; Zhu, X.; Xiong, J.; Wen, Z.; Cheng, G. A p–n Junction by Coupling Amine-Enriched Brookite–TiO_2 Nanorods with Cu_xS Nanoparticles for Improved Photocatalytic CO_2 Reduction. *Materials* **2023**, *16*, 960. https://doi.org/10.3390/ma16030960

Academic Editor: Roberta G. Toro

Received: 23 December 2022
Revised: 14 January 2023
Accepted: 17 January 2023
Published: 19 January 2023

1. Introduction

The excessive emission of CO_2 resulting from the acceleration of industrialization and use of fossil fuel has caused global warming and serious environmental problems [1]. Photocatalytic CO_2 reduction, denoted as "artificial photosynthesis", is a promising technology for CO_2 conversion [2–4]. It is critical to develop efficient photocatalysts through surface and interface engineering [5,6]. Semiconductor TiO_2 has attracted extensive attention concerning CO_2 photoreduction owing to its stability, low cost, and low toxicity. However, TiO_2 is an n-type semiconductor with a wide band gap, and the disadvantages of limited light harvesting and poor electron–hole pair separation are not conducive to highly efficient photocatalytic CO_2 reduction [7–9].

Construction of a p–n junction is one promising approach to facilitate the separation of photogenerated carriers and improve the utilization of solar energy [10–13]. Fan et al. reported that 3D CuS@$ZnIn_2S_4$ p–n heterojunctions with 2D/2D nanosheet subunits can promote the separation of photogenerated carriers and accelerate carrier transfer [14]. Yu et al. suggested that a CuO/TiO_2 p–n heterojunction can improve the separation efficiency of photogenerated electron–hole pairs [15]. It is well known that CuS and Cu_2S are p-type semiconductors with narrow bandgaps [16,17]. When coupling Cu_xS with TiO_2, upon light irradiation, an internal electric field is established with the formation of a p–n heterojunction. Accordingly, the lower flat band potential of Cu_xS allows for the

transfer of photoexcited electrons from Cu_xS to TiO_2, while the holes diffuse from TiO_2 to Cu_xS [18,19], which could suppress the charge recombination to achieve an efficient separation of electrons and holes during the photocatalytic process. In this regard, the formation of a TiO_2/Cu_xS p–n junction has potential for improving photocatalytic CO_2 reduction. However, most of the studies upon TiO_2/CuS p–n junctions focus on the applications of photocatalytic pollution degradation and hydrogen (H_2) energy generation from water [19–22]. There are few works relevant to photocatalytic CO_2 reduction by designing TiO_2/CuS composites. Recently, Lee et al. [23] reported a CuS_x-TiO_2 film could effectively promote photogenerated charge separation for CO_2 photoreduction. It is still a challenge to rationally design CuS_x-TiO_2 p–n junctions for efficient CO_2 photoreduction.

Due to the unique surface state and higher conduction band position of brookite TiO_2 compared to anatase and rutile [24,25], great potential has emerged in the field of photocatalytic CO_2 reduction. Liu et al. reported that defective brookite TiO_2 had the highest yield for CO and CH_4 production among the three TiO_2 polymorphs [26]. Subsequently, Peng's group studied exposed-crystal-face controlling [27], the construction of heterojunctions [28], and supported metal cocatalysts and dual cocatalysts [29,30] to improve the CO_2 photoreduction activity of brookite TiO_2. In fact, the activation and adsorption of CO_2 are significant factors to enhance CO_2 photoreduction [31–33]. Surface amine modification has attracted great attention in this issue, because the amine groups can not only promote the adsorption and activation of CO_2, but also coordinate with other metal ions to bind closely. Jin et al. [32] reported that surface amine modification enhances the activity of metal@TiO_2 photocatalysts. On the basis of the above backgrounds, in this work, amine-modified brookite TiO_2 nanorods coupled with Cu_xS nanoparticles has been successfully fabricated. A significant p–n junction is formed between the NH_2-B-TiO_2-Cu_xS interface, which effectively improves the transfer and separation of charge carriers. The composition and morphology of NH_2-B-TiO_2 are characterized and the improved performance of photocatalytic CO_2 reduction is also discussed.

2. Experimental

2.1. Reagents

All the analytical reagents were used without advance refinement. Tetrabutyl titanate (TBOT), thioacetamide (TAA) and copper (II) acetate monohydrate ($Cu(CH_3COO)_2 \cdot H_2O$) were purchased from Aladdin in China. Ethanediamine (EDA), ethylene glycol (EG) and absolute ethyl alcohol were provided by Sinopharm Chemical Reagent Co., Ltd. (Shanghai, China). All the experiments were conducted with deionized water.

2.2. Materials Synthesis

Synthesis of amine-modified brookite TiO_2 (NH_2-B-TiO_2): First, titanium glycolate precursor was synthesized based on our previous reports [34–36]; 5 mL tetrabutyl titanate (TBT) was placed into a round-bottomed flask containing 180 mL ethylene glycol (EG) and swirled with magnetic force for 1 h at 120 °C. The white powder material was washed five times with deionized water and once with anhydrous ethanol before being dried at 60 °C for 48 h. To make amine-modified brookite TiO_2, 0.5 g of the as-prepared titanium glycolate precursor was disseminated in 35 mL of deionized water and 35 mL of ethylenediamine by ultrasonic treatment, and this mixture was uniformly transferred to a 100 mL Teflon-lined stainless-steel autoclave and then placed in an oven at 180 °C for 12 h. Following filtration and washing with deionized water 5 times and with anhydrous ethanol once, finally, the product was gathered after drying at 60 °C for 12 h.

Synthesis of brookite TiO_2 (B-TiO_2): Thus method is similar to the method used to prepare amine-modified brookite TiO_2. Firstly, titanium glycolate precursor was synthesized and then 0.5 g of the as-prepared titanium glycolate precursor was dispersed in 64 mL of deionized water and 6 mL NaOH (1 mol/L) using ultrasonic treatment, which was evenly transferred to a 100 mL Teflon-lined stainless-steel autoclave and later heated at 180 °C for

12 h. Following filtration and washing with deionized water and anhydrous ethanol to pH = 7, the product was gathered and dried at 60 °C for 12 h.

Synthesis of Cu_xS particles: First, 100 mg $Cu(CH_3COO)_2 \cdot H_2O$ (0.5 mmol) was added to a round-bottomed flask containing 20 mL of anhydrous ethanol in an oil bath held at 80 °C under magnetic stirring, to which 42 mg of TAA was added, and kept at reflux for 4 h. The obtained product was centrifuged and washed numerous times with distilled water and anhydrous alcohol.

Synthesis of NH_2-B-TiO_2-Cu_xS: As-synthesized NH_2-B-TiO_2 (12.5, 25, 50 mg, respectively) and 10 mg $Cu(CH_3COO)_2 \cdot H_2O$ were added to a round-bottomed flask containing 20 mL of anhydrous ethanol in an oil bath held at 80 °C under magnetic stirring, then we added 42 mg of TAA and kept at reflux for 4 h. Then, the suspension was washed with distilled water and distilled alcohol several times via centrifugation. Finally, the obtained product was dried at 60 °C for 12 h. Different ratios of NH_2-B-TiO_2-Cu_xS composites were denoted as NH_2-B-TiO_2-Cu_xS-n, where n represented the molar ratio of Cu_xS, and the values of n were 8, 16, and 32, respectively.

2.3. Characterization of Photocatalysts

X-ray powder diffraction (XRD) measurements were carried out on an Ultima IV X-ray diffractometer with Cu Kα radiation in a range of 10–80° and the scan rate was 10°/min at 40 kV and 30 mA. Fourier-transform infrared (FT-IR) spectra were collected on a Nicolet iS10 IR spectrometer to analyze the chemical bonds and functional groups of the material. Scanning electron microscopy (SEM) and energy-dispersive X-ray spectroscopy (EDX) techniques on a JSM 2100 electron microscope operating at a 200 kV accelerating voltage were used to display the morphologies and elemental dispersion of the samples. X-ray photoelectron spectroscopy (XPS) spectra were measured using Thermo Scientific K-Alpha with an Al Kα X-ray sources (hν = 1486.6 eV, 12 kV 6 mA). All binding energies were calibrated through the C 1s peak at 284.8 eV. UV–vis diffuse reflectance spectrum (UV–vis DRS) was investigated on a Shimadzu UV-2550 spectrometer in a range of 200–800 nm. The photocurrent and electrochemical impedance measurements were performed on a CHI 760E electrochemical workstation, including a standard three-electrode system in 0.2 M Na_2SO_4 solution, where Pt wire, $Hg/HgCl_2$, and the as-prepared product were used as counter electrode, reference electrode, and working electrode, respectively. Mott–Schottky (M-S) and photocurrent decay plots were also carried out on a CHI 760E electrochemical workstation in 0.2 M Na_2SO_4 solution. Among them, the preparation process of the working electrode involved weighing 10 mg of the sample in the sample tube and then adding 1 mL N, N dimethylformamide (DMF) and 20 μL Dupont Nafion membrane solution, which was then stirred for 30 min; after it was completely uniform, we used a pipette gun to transfer 30 μL of the mixed solution coated on the FTO conductive glass. Finally, it was dried in a vacuum oven.

2.4. Evaluation of Photocatalytic CO_2 Reduction

The photocatalytic reduction of CO_2 was evaluated under irradiation of 300 W xenon lamp and its wavelength was used to simulate sunlight in a gas-closed quartz reactor with a volume of 200 mL. Typically, 50 mg of the as-prepared catalyst was dispersed completely in 1 mL of deionized water in a glass Petri dish, which was then transferred to a quartz reactor with a bottom of 10 mL of deionized water. The reactor was bubbled with high-purity CO_2 gas for half an hour and the air inside was exhausted prior to illumination. Then, the reaction system was sealed and we turned on the xenon lamp. Subsequently, 1 mL of gaseous product was extracted from the glass reactor by a sampling needle every 1 h, and an irradiation duration of 4 h was applied and analyzed using a gas chromatograph (GC-7900, CEAULIGHT Beijing, China) equipped with an FID detector while N_2 gas served as the carrier gas. The reactor temperature was maintained at 25 °C and atmospheric pressure after starting the photocatalytic reaction.

3. Results and Characterization

The formation process of Cu_xS particles supported on amine-modified brookite nanorods is shown in Figure 1. Firstly, the titanium glycolate precursor is synthesized by a simple reflux method. Subsequently, ethylenediamine is introduced to prepare amine-modified brookite TiO_2 nanorods via a hydrothermal method. Finally, Cu_xS nanoparticles are deposited on the as-synthesized brookite TiO_2 nanorods by a refluxing method using copper acetate monohydrate and thioacetamide (TAA) as the precursors.

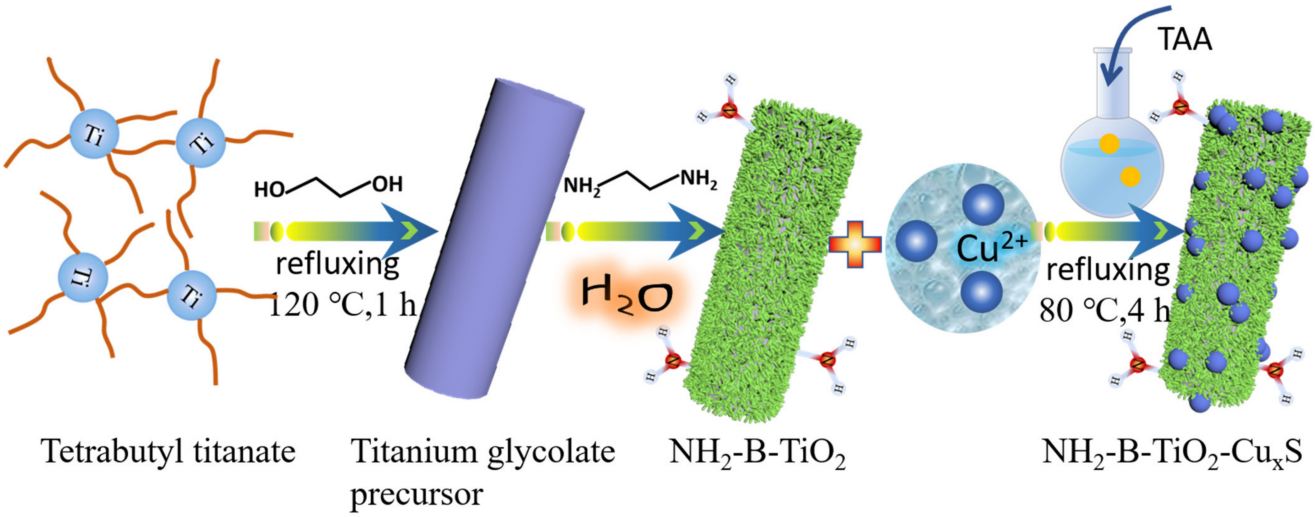

Figure 1. Illustration of the NH_2-B-TiO_2-Cu_xS composites process.

Figure 2a shows the X-ray diffraction (XRD) pattern of the as-prepared samples to analyze the composition of the sample. It can be seen that the prepared pure brookite TiO_2 matches well with the standard one (JCPDF No. 15-875), while the obtained Cu_xS corresponds to a mixture of the CuS phase (JCPDF No.65-3588) and low-chalcocite Cu_2S phase (JCPDF No. 65-3816). It can be found that the peaks of brookite TiO_2 appear in all the as-prepared composites. However, the peaks of Cu_xS can only be found in the NH_2-B-TiO_2-Cu_xS 32% sample, which may be due to the strong diffraction peaks of brookite TiO_2 and low contents of Cu_xS particles in this composite. The UV-Vis absorption (UV-DRS) spectra of the as-synthesized materials are displayed in Figure 2b. It became apparent that the pristine NH_2-B-TiO_2 has an absorption edge at around 390 nm. However, the NH_2-B-TiO_2-Cu_xS composites show red shift to the visible light region (400–800 nm), and the light absorption intensity gradually increases with the increase in Cu_xS loading. Further, the Fourier-transform infrared (FT-IR) is used to analyze the chemical bonds and functional groups of the sample. Figure 2c shows FT-IR spectra of the NH_2-B-TiO_2 and NH_2-B-TiO_2-Cu_xS-16% samples, in which the brookite TiO_2 (B-TiO_2) (XRD in Figure 2d) is also prepared in the presence of NaOH for comparison. Indeed, the B-TiO_2 has no amine modification, while the NH_2-B-TiO_2 and NH_2-B-TiO_2-Cu_xS samples have two new peaks located at ~1620 and ~3400 cm^{-1}, respectively, which may be attributed to the N–H bending vibration and N–H stretching vibration, respectively [37,38].

To further confirm the composition of the sample, X-ray photoelectron spectroscopy (XPS) analysis was also performed to study the composition and surface chemical status of samples. Figure 3a shows the full XPS survey spectra of the NH_2-B-TiO_2, Cu_xS, and NH_2-B-TiO_2-Cu_xS samples. Among them, the full XPS survey spectra of the NH_2-B-TiO_2-Cu_xS composite confirms the existence of N, Ti, O, Cu, and S elements. In Figure 3d, for N 1s in NH_2-B-TiO_2, the binding energy peak at 400 and 401.2 is attributed to the NH_2 group and N-H bonds [37,39], respectively, which suggests amine modification was achieved. After loading Cu_xS, the N 1s peak shifted positively and it was proposed that the amines donate their lone pair of electrons on N atoms to Cu. For NH_2-B-TiO_2, the high-resolution XPS spectra of Ti 2p are shown in Figure 3b, and two tiny peaks observed at 458.6 and

464.3 eV are related to Ti $2p_{3/2}$ and Ti $2p_{1/2}$, respectively, which indicates the presence of Ti^{4+} [40,41]. Furthermore, Figure 3c exhibits two peaks located at 529.8 and 530.7 eV, which correspond to lattice oxygen and chemisorbed and dissociated oxygen, respectively [42–44]. For Cu_xS, as shown in Figure 3e, the peaks at 932.6 and 952.7 eV belong to Cu $2p_{1/2}$ and Cu $2p_{3/2}$ of Cu^+ species, respectively [45,46], while the peak positions at 935.6 and 955.6 eV are consistent with Cu $2p_{3/2}$ and Cu $2p_{1/2}$ of Cu^{2+} [47]. These characteristic peaks with a spin–orbit separation of 20 eV indicate the presence of Cu^{2+} ions [16]. In addition, the other two satellite peaks of Cu^+ and Cu^{2+} appear at 940.7 and 944.7 eV, respectively. Figure 3f displays the high-resolution spectrum at the S 2p region. The typical peak at 162.3 eV is from S 2p of S^{2-} [48,49]; moreover, a small peak at 169.1 eV is ascribed to SO_4^{2-}, which is due to S^{2-} being oxidized partially [50,51]. However, in the NH_2-B-TiO_2-Cu_xS composite, all the binding energies of Ti, O, and N shift to higher regions, whereas Cu and S shift to lower binding energies compared with the pristine TiO_2 and Cu_xS. It might be attributed to chemical interaction and electron transfer in the p–n junction formed at the interface of NH_2-B-TiO_2 and Cu_xS [52].

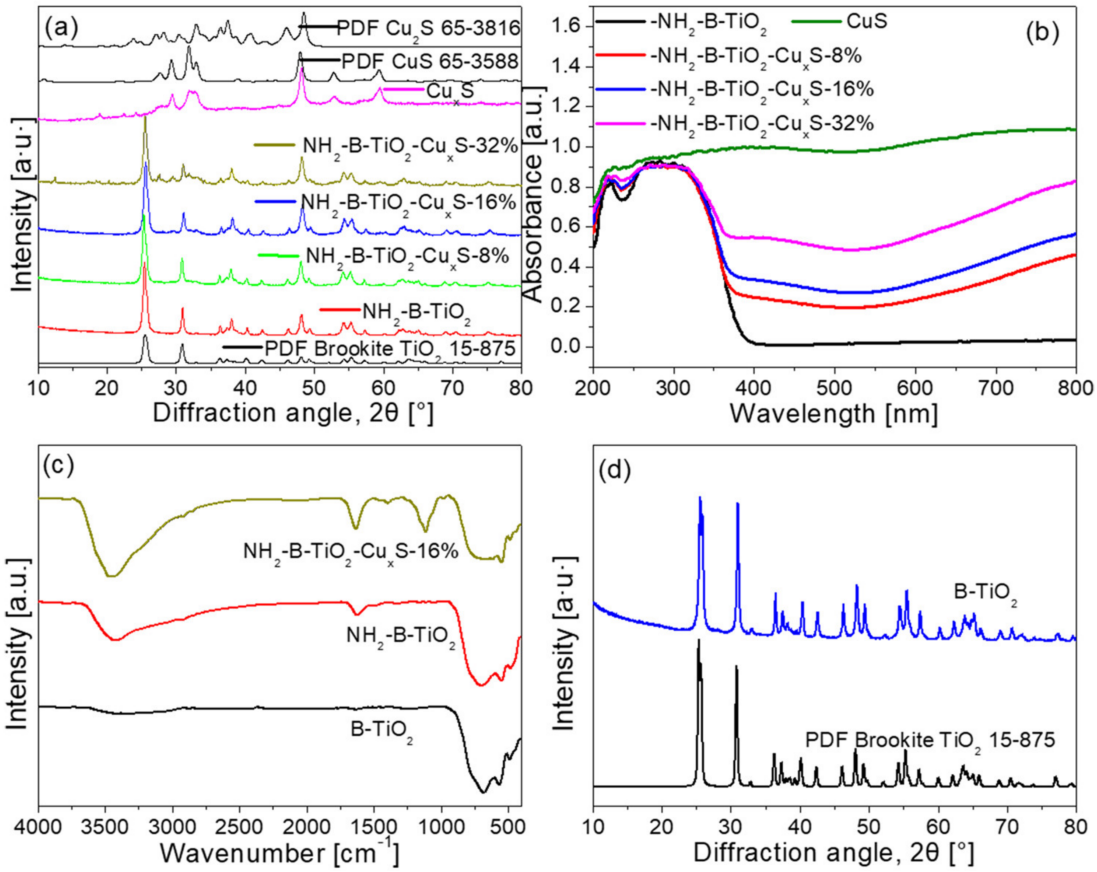

Figure 2. (**a**) XRD patterns of the NH_2-B-TiO_2-Cu_xS composites; (**b**) UV-DRS spectra of the NH_2-B-TiO_2, Cu_xS, and NH_2-B-TiO_2-Cu_xS composites; (**c**) FTIR spectra of B-TiO_2, NH_2-B-TiO_2, and NH_2-B-TiO_2-Cu_xS-16%; (**d**) XRD pattern of brookite TiO_2 (B-TiO_2).

The morphology structures of the as-prepared materials are further determined by SEM. Figure 4a shows that the as-prepared NH_2-B-TiO_2 is a rod-like structure with a diameter of 600–800 nm and a length of 2.5–3.5 μm. It can be observed that the microrods assemble with many tiny nanoparticles distributed on the surface. Figure 4b is an SEM image of Cu_xS, in which the size and morphology are difficult to determine due to the phenomenon of particle aggregation. As shown in Figure 4c, Cu_xS particles are dispersed on the surface of NH_2-B-TiO_2 nanorods. In addition, energy-dispersive X-ray spectroscopy (EDX) mapping images of the NH_2-B-TiO_2-Cu_xS composites show the presence and even

distribution of Ti, O, N, Cu, and S elements on the surface of the nanorod in Figure 4d–i, which further confirms that NH_2-B-TiO_2 and Cu_xS are hybridized uniformly.

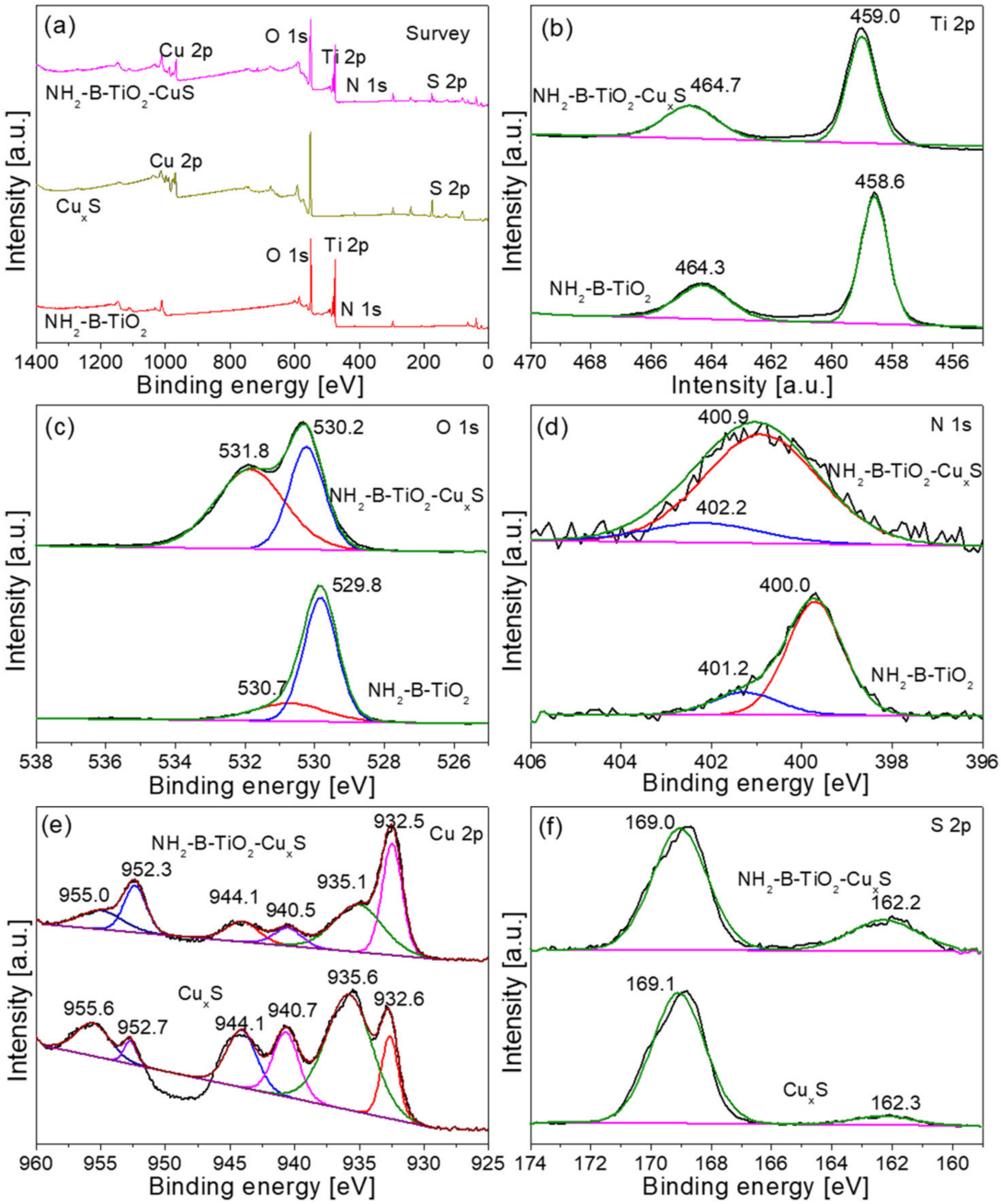

Figure 3. (**a**) XPS survey spectra of NH_2-B-TiO_2, Cu_xS, and NH_2-B-TiO_2-Cu_xS-16% samples; XPS spectra of (**b**) Ti 2p, (**c**) O 1s, (**d**) N 1s, (**e**) Cu 2p and (**f**) S 2p for different materials.

In order to explore further CO_2 photoconversion efficiency, the photocatalytic CO_2 reduction performances of the as-obtained materials are evaluated in the presence of H_2O using a gas chromatograph. As shown in Figure 5a, under the irradiation of a 300 W xenon lamp, only CH_4 was detected in the photocatalytic process of all samples, which may be because the prepared materials only meet the reduction potential of CO_2 reduction to CH_4 ($E^0 = -0.24$ eV). All the samples have the activity of photocatalytic reduction of CO_2 into CH_4, except for the bare Cu_xS. Among those samples, the brookite TiO_2 modified with amines (NH_2-B-TiO_2) has superior capability to that of B-TiO_2, indicating that amine modification has a positive effect on the reduction of CO_2 to CH_4. With loading

of Cu_xS nanoparticles, the NH_2-B-TiO_2-Cu_xS composites have enhanced performances for photocatalytic CO_2 reduction into CH_4. In particular, the NH_2-B-TiO_2 shows a low CH_4 production rate of about 0.73 μmol g^{-1} h^{-1}, while the optimized NH_2-B-TiO_2-Cu_xS-16% sample has a yield rate of 3.34 μmol g^{-1} h^{-1}, which is 4-fold more than that of the pure NH_2-B-TiO_2. Those results suggest that the Cu_xS could act as a cocatalyst in the amine-enriched B-TiO_2-Cu_xS composite for improvements in photocatalytic CO_2 reduction compared to pristine ones. Typically, to evaluate the stability of the as-synthesized photocatalyst, the photocatalytic CO_2 reduction activity with five-run cycling of the NH_2-B-TiO_2-Cu_xS 16% sample is tested (Figure 5b). It can be found that the activity of CO_2 photoconversion to CH_4 is unstable, and the yield of CH_4 production gradually decreases, which could be attributed to the deactivation of the composite resulting from the oxidation of Cu_xS.

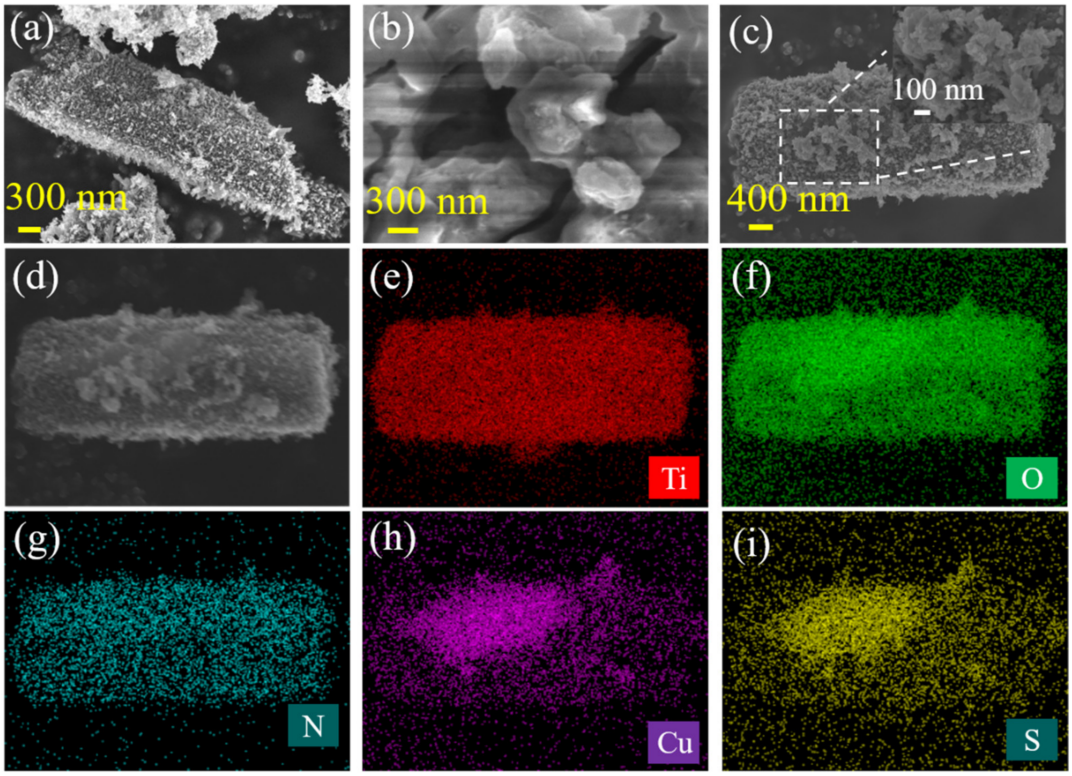

Figure 4. SEM images of (**a**) NH_2-B-TiO_2, (**b**) Cu_xS, and (**c**) NH_2-B-TiO_2-Cu_xS-32% samples; (**d**–**i**) EDX mapping images of the NH_2-B-TiO_2-Cu_xS-32%.

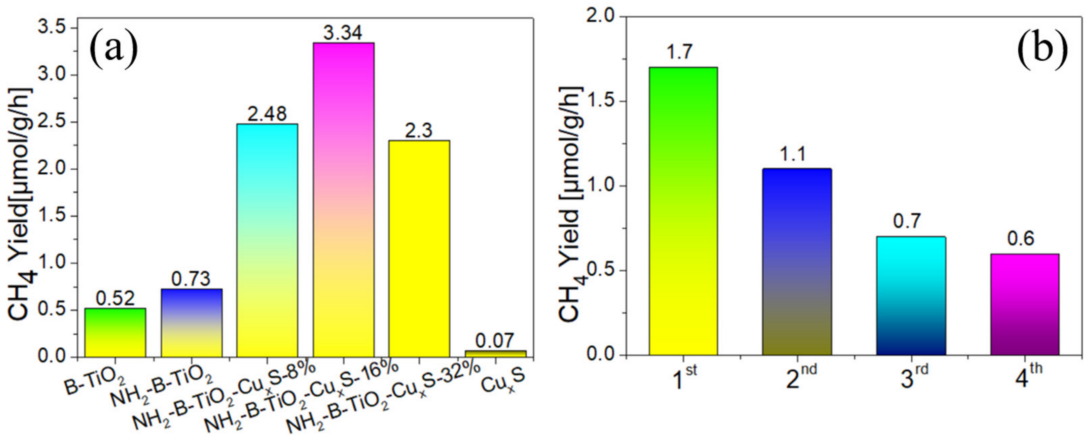

Figure 5. (**a**) Photocatalytic CO_2 reduction activity of NH_2-B-TiO_2, Cu_xS and NH_2-B-TiO_2-Cu_xS composites. (**b**) Stability of CO_2 photoconversion in NH_2-B-TiO_2-Cu_xS samples.

Figure 6 shows the XPS spectra of Cu 2p of the NH_2-B-TiO_2-Cu_xS 16% sample after the photocatalytic reaction. It can be observed that the valence state of copper displays obvious changes. The binding energies of 932.7 and 952.7 eV are ascribed to Cu $2p_{3/2}$ and Cu $2p_{1/2}$, respectively, a typical peak location of Cu^{2+} in CuS [14,20]. A weak satellite peak around 944 eV further indicates the presence of Cu^{2+} [53]. These results indicate that Cu^{+} was completely oxidized to Cu^{2+} after the photocatalytic reaction in this photocatalysis system, which might weaken the cycling performance of the NH_2-B-TiO_2-Cu_xS composite.

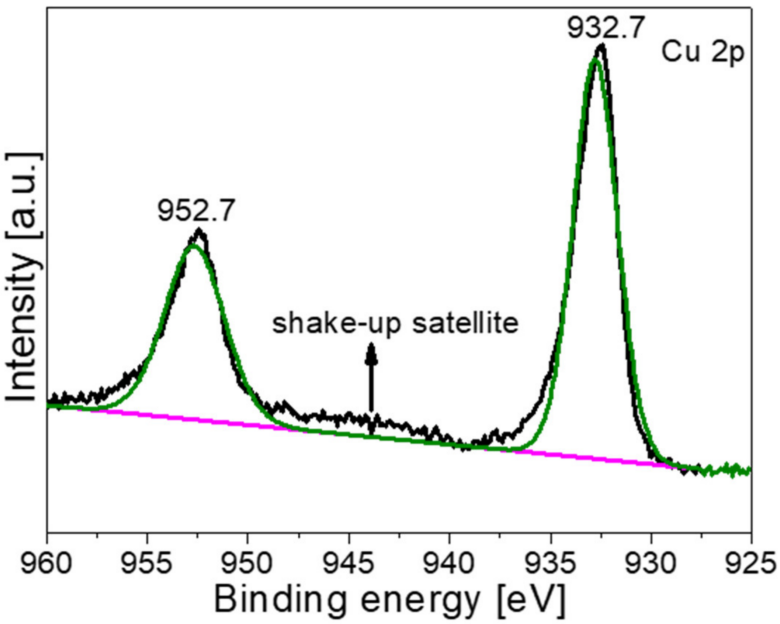

Figure 6. XPS spectra of Cu 2p after the photocatalytic reaction.

As a matter of fact, as shown in the Mott–Schottky curve in Figure 7a–c, the slope of NH_2-B-TiO_2 is positive, suggesting an n-type semiconductor [54]. At the same time, the slope of Cu_xS is negative, suggesting that Cu_xS is an p-type semiconductor. However, the NH_2-B-TiO_2-Cu_xS-16% composite exhibits an inverted "V- shape", being a symbol of a typical p–n junction [55,56], which indicates that a p–n heterojunction could be constructed between the NH_2-B-TiO_2 and Cu_xS. In addition, the formation of the p–n heterojunction is further confirmed by valence band (VB)-XPS and core-level spectrum analyses. As shown in Figure 7d–f, the band alignment of NH_2-B-TiO_2 and Cu_xS between the NH_2-B-TiO_2-Cu_xS heterojunction interface can be calculated according to the following: Equations (1)–(3) [57].

$$\Delta E_{VBO} = \left(E_{CL}^{Cu_xS} - E_{VBM}^{Cu_xS}\right) - \left(E_{CL}^{TiO_2} - E_{VBM}^{TiO_2}\right) + \Delta E_{CL}^{Int} \quad (1)$$

$$\Delta E_{CL}^{Int} = \left(E_{CL}^{TiO_2} - E_{CL}^{Cu_xS}\right)^{NH_2-B-TiO_2-CuxS-16\%} \quad (2)$$

$$\Delta E_{CBO} = E_g^{CuxS} - E_g^{TiO_2} \quad (3)$$

In the above equations, the ΔE_{VBO} represents the valence band offset, which is the energy difference between the core energy level (E_{CL}) and the valence band maximum (E_{VBM}) in a pure material; meanwhile, ΔE_{CL}^{Int} illuminates the energy difference between the core levels. ΔE_{CBO} represents the conduction band offset. Further, the band gap of the as-synthesized materials is calculated according to the Kubelka–Munk function in Figure 8a,b [58,59], and the band gap energies of pure NH_2-B-TiO_2 and Cu_xS are 3.14 and 2.04 eV, respectively. Based on the information reflected from the XPS and DRS analyses, Figure 8e reveals ΔE_{VBO} = 2.38 eV and ΔE_{CBO} = 1.28 eV for the NH_2-B-TiO_2-Cu_xS nanocomposite. The VB-XPS spectra are verified, as shown in Figure 8c,d, as the valence band position for NH_2-B-TiO_2 and Cu_xS is 2.74 and 1.48 eV, respectively [60]. Therefore, the

conduction band position of NH_2-B-TiO_2 and Cu_xS can be calculated as −0.4 and −0.56, respectively. In this regard, the formation of such a p–n junction and the resulting charge transfer are shown in Figure 8e. After contact, the Fermi levels of NH_2-B-TiO_2 and Cu_xS move down and up, respectively, until an equilibrium state is reached. When a built-in electric field between the NH_2-B-TiO_2 and Cu_xS interface is established, this allows for the electrons in Cu_xS to migrate to NH_2-B-TiO_2 while the holes in NH_2-B-TiO_2 are transferred to the Cu_xS. It is proposed that Cu_xS as a cocatalyst promotes the efficient separation of photogenerated charge carriers.

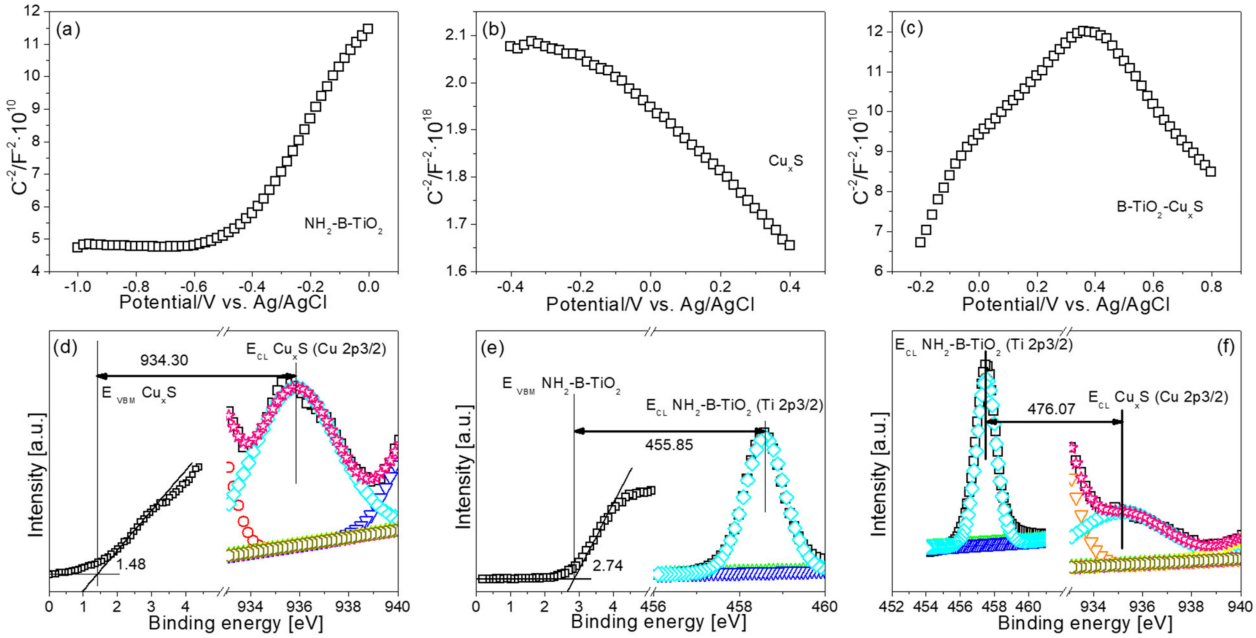

Figure 7. Mott-Schottky plots of (**a**) pure NH_2-B-TiO_2, (**b**) Cu_xS particles, (**c**) NH_2-B-TiO_2-16%; VB-XPS and core-level spectrum of (**d**) Cu_xS and (**e**) NH_2-B-TiO_2; (**f**) XPS core-level spectrum of NH_2-B-TiO_2-16%.

Generally, the separation efficiency of photogenerated electrons and holes has a significant impact on the photocatalytic performance [61–63]. Herein, photo/electrochemical measurements are carried out to study the charge transfer of the as-synthesized materials. In Figure 9a, the photocurrent density of the NH_2-B-TiO_2-Cu_xS-16% composite is higher than pure NH_2-B-TiO_2, which indicates that the loading of Cu_xS can effectively prevent recombination of the photogenerated electrons and holes. As shown in Figure 9b, the semicircle radius of the NH_2-B-TiO_2-Cu_xS-16% sample is smaller than that of pure NH_2-B-TiO_2, implying that the charge carriers have a rapid transfer rate on the composite.

Based on the above results and discussions, a possible CO_2 photoreduction process is proposed in Figure 9c. Before the photoreduction reaction, the surface amine modification is helpful for the adsorption and activation of CO_2 [31,37]. Under irradiation of a light source, n-type (NH_2-B-TiO_2) and p-type semiconductors (Cu_xS) generate photogenerated electrons in the conduction band (CB) and holes in the valence band (VB). The CB of NH_2-B-TiO_2 is more positive than that of Cu_xS, and the VB of Cu_xS is more negative than that of NH_2-B-TiO_2. After contact between NH_2-B-TiO_2 and the Cu_xS interface, the built-in electric field is established, which promotes the migration of photoexcited electrons from the CB of Cu_xS to NH_2-B-TiO_2 and the migration of holes from the VB of NH_2-B-TiO_2 to Cu_xS, and these facilitate the separation and transfer of photogenerated electrons and holes. Further, the rate of reduction of CO_2 to CH_4 by the photoinduced electrons in CB of NH_2-B-TiO_2 is improved.

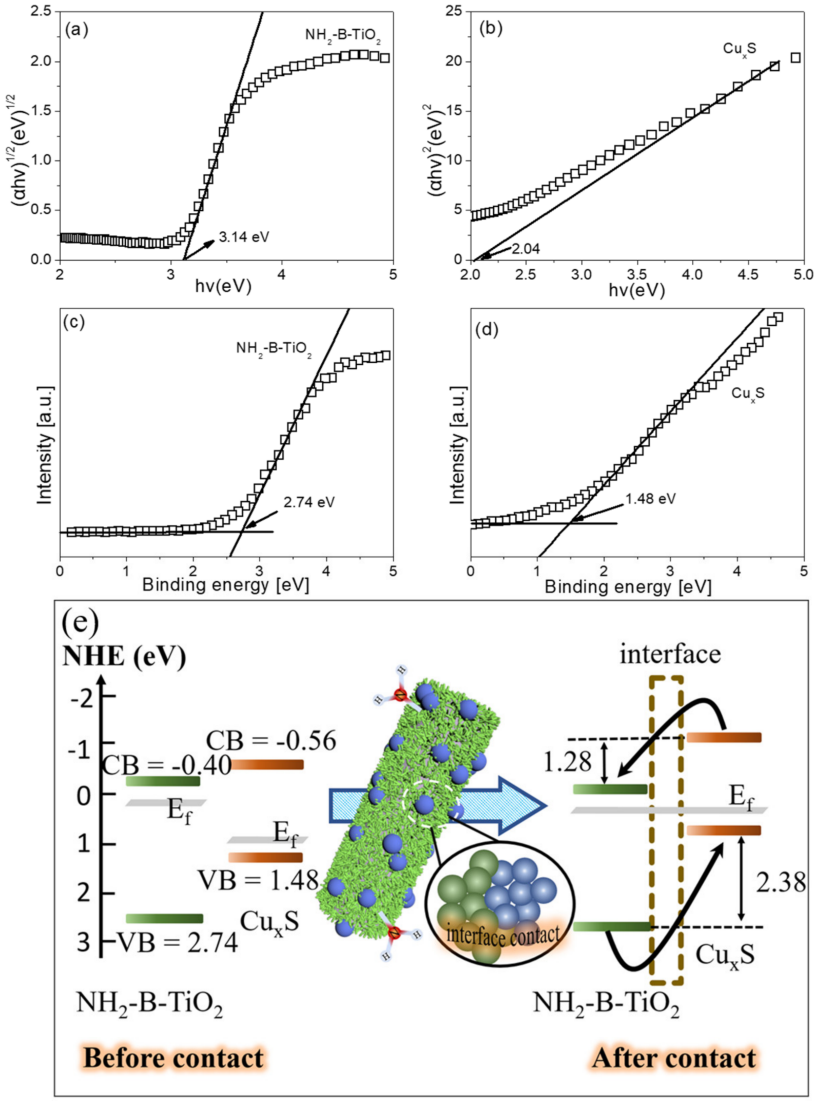

Figure 8. The plot of transformed Kubelka-Munk function of (**a**) NH_2-B-TiO_2 and (**b**) Cu_xS. The valance-band XPS spectrum of (**c**) NH_2-B-TiO_2 and (**d**) Cu_xS; (**e**) schematic illustration for formation of p-n junction on the NH_2-B-TiO_2-Cu_xS composite.

As shown in Table 1, the CO_2 photoreduction activity of the NH_2-B-TiO_2-Cu_xS composite is higher than that of other TiO_2-based binary and ternary composites reported previously.

Table 1. A comparative study on photocatalytic CO_2 reduction upon different photocatalysts.

Photocatalyst	Light Source	Reaction Condition	CH4 Production Rate [μmol/g/h]	References
NH_2-B-TiO_2-Cu_xS	300 W Xe lamp	H_2O vapor	3.34	This work
Pt-Cu_2O/TiO_2	300 W Xe lamp	H_2O vapor	1.42	[64]
TiO_2/g-C_3N_4	300 W Xe lamp	H_2O vapor	2.50	[28]
Au@TiO_2	300 W Xe lamp	H_2O vapor	2.52	[65]
CdS/rGO/TiO_2	300 W Xe lamp	H_2O vapor	0.063	[66]
Mg-TiO_2	300 W Xe lamp	H_2O vapor	1.0	[67]

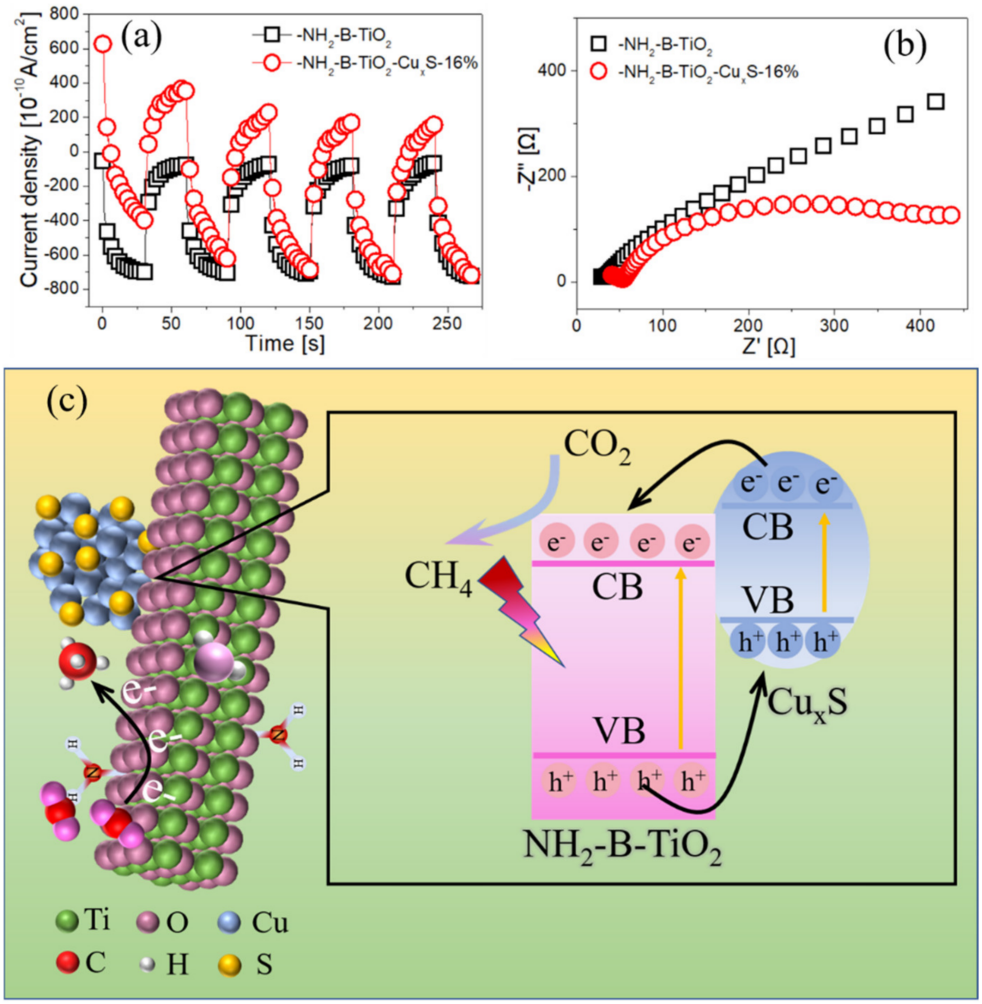

Figure 9. (**a**) Transient photocurrent responses and (**b**) Nyquist plots of NH_2-B-TiO_2 and NH_2-B-TiO_2-Cu_xS-16%; (**c**) possible photocatalytic CO_2 reduction process for the NH_2-B-TiO_2-Cu_xS composite.

4. Conclusions

In summary, an amine-enriched p–n junction upon the NH_2-B-TiO_2-Cu_xS composite was successfully prepared. The modification of amine on the surface of the photocatalyst has a positive effect on the enhancement of CO_2 activity. The photocatalytic CO_2 reduction activity of amine-modified brookite TiO_2 is higher than that of amine-free modified brookite TiO_2. Further, coupling different contents of Cu_xS with NH_2-B-TiO_2, the NH_2-B-TiO_2-Cu_xS-16% composite exhibits the greatest CH_4 yield rate of 3.34 μmol g^{-1} h^{-1} following 4 h of lighting, which is 4 times higher than that of pure NH_2-B-TiO_2. Combining the valence band XPS spectra with photo/electrochemical measurements, the formation of a p–n junction between the NH_2-B-TiO_2-Cu_xS interface was confirmed. With the formation of such a heterojunction, the recombination of photogenerated electrons and holes is inhibited, thereby greatly improving the photocatalytic CO_2 reduction activity. It is hoped that this work could provide an approach to construct amine-enriched p–n junctions for efficient CO_2 photoreduction.

Author Contributions: Methodology, J.X.; Formal analysis, X.Z. and Z.W.; Writing—original draft, Z.C.; Writing—review & editing, G.C. All authors have read and agreed to the published version of the manuscript.

Funding: This research was funded by the Graduate Innovative Fund of Wuhan Institute of Technology (NO. CX2021336).

Institutional Review Board Statement: Not applicable.

Informed Consent Statement: Not applicable.

Data Availability Statement: All relevant data are contained in the present manuscript.

Conflicts of Interest: The authors declare no conflict of interest.

References

1. Ahmad, T.; Liu, S.; Sajid, M.; Li, K.; Ali, M.; Liu, L.; Chen, W. Electrochemical CO_2 reduction to C^2 products using Cu-based electrocatalysts: A review. *Nano Res. Energy* **2022**, *1*, e9120021. [CrossRef]
2. Lu, K.-Q.; Li, Y.-H.; Zhang, F.; Qi, M.-Y.; Chen, X.; Tang, Z.-R.; Yamada, Y.M.A.; Anpo, M.; Conte, M.; Xu, Y.-J. Rationally designed transition metal hydroxide nanosheet arrays on graphene for artificial CO_2 reduction. *Nat. Commun.* **2020**, *11*, 5181. [CrossRef] [PubMed]
3. Kong, T.; Jiang, Y.; Xiong, Y. Photocatalytic CO_2 conversion: What can we learn from conventional CO_x hydrogenation? *Chem. Soc. Rev.* **2020**, *49*, 6579–6591. [CrossRef] [PubMed]
4. Yin, S.; Zhao, X.; Jiang, E.; Yan, Y.; Zhou, P.; Huo, P. Boosting water decomposition by sulfur vacancies for efficient CO_2 photoreduction. *Energy Environ. Sci.* **2022**, *15*, 1556–1562. [CrossRef]
5. Liu, L.; Wang, S.; Huang, H.; Zhang, Y.; Ma, T. Surface sites engineering on semiconductors to boost photocatalytic CO_2 reduction. *Nano Energy* **2020**, *75*, 104959. [CrossRef]
6. Li, X.; Yu, J.; Jaroniec, M.; Chen, X. Cocatalysts for Selective Photoreduction of CO_2 into Solar Fuels. *Chem. Rev.* **2019**, *119*, 3962–4179. [CrossRef]
7. Yu, Y.; Dong, X.; Chen, P.; Geng, Q.; Wang, H.; Li, J.; Zhou, Y.; Dong, F. Synergistic Effect of Cu Single Atoms and Au–Cu Alloy Nanoparticles on TiO2 for Efficient CO_2 Photoreduction. *ACS Nano* **2021**, *15*, 14453–14464. [CrossRef] [PubMed]
8. Li, M.; Liu, Z.; Wu, S.; Zhang, J. Advances for CO_2 Photocatalytic Reduction in Porous Ti-Based Photocatalysts. *ACS EST Eng.* **2022**, *2*, 942–956. [CrossRef]
9. Qiu, P.; Lu, M.; Cheng, G.; Li, W.; Liu, L.; Xiong, J. Co-implantation of oxygen vacancy and well-dispersed Cu cocatalyst into TiO_2 nanoparticles for promoting solar-to-hydrogen evolution. *Int. J. Hydrog. Energy* **2023**, *48*, 933–942. [CrossRef]
10. Jiang, L.; Wang, K.; Wu, X.; Zhang, G. Highly Enhanced Full Solar Spectrum-Driven Photocatalytic CO_2 Reduction Performance in $Cu_{2-x}S/g\text{-}C_3N_4$ Composite: Efficient Charge Transfer and Mechanism Insight. *Sol. RRL* **2021**, *5*, 2000326. [CrossRef]
11. Qiu, P.; Xiong, J.; Lu, M.; Liu, L.; Li, W.; Wen, Z.; Li, W.; Chen, R.; Cheng, G. Integrated p-n/Schottky junctions for efficient photocatalytic hydrogen evolution upon $Cu@TiO_2\text{-}Cu_2O$ ternary hybrids with steering charge transfer. *J. Colloid Interface Sci.* **2022**, *622*, 924–937. [CrossRef] [PubMed]
12. Yang, G.; Qiu, P.; Xiong, J.; Zhu, X.; Cheng, G. Facilely anchoring Cu_2O nanoparticles on mesoporous TiO_2 nanorods for enhanced photocatalytic CO_2 reduction through efficient charge transfer. *Chin. Chem. Lett.* **2022**, *33*, 3709–3712. [CrossRef]
13. Ávila-López, M.A.; Tan, J.Z.Y.; Luévano-Hipólito, E.; Torres-Martínez, L.M.; Maroto-Valer, M.M. Production of CH_4 and CO on CuxO and NixOy coatings through CO_2 photoreduction. *J. Environ. Chem. Eng.* **2022**, *10*, 108199. [CrossRef]
14. Fan, H.-T.; Wu, Z.; Liu, K.-C.; Liu, W.-S. Fabrication of 3D $CuS@ZnIn_2S_2$ hierarchical nanocages with 2D/2D nanosheet subunits p-n heterojunctions for improved photocatalytic hydrogen evolution. *Chem. Eng. J.* **2022**, *433*, 134474. [CrossRef]
15. Yu, D.; Xu, L.; Zhang, H.; Li, J.; Wang, W.; Yang, L.; Jiang, X.; Zhao, B. A new semiconductor-based SERS substrate with enhanced charge collection and improved carrier separation: CuO/TiO_2 p-n heterojunction. *Chin. Chem. Lett.* **2022**, 107771. [CrossRef]
16. Neelgund, G.M.; Oki, A. Folic acid and CuS conjugated graphene oxide: An efficient photocatalyst for explicit degradation of toxic dyes. *Appl. Surf. Sci.* **2021**, *566*, 150648. [CrossRef]
17. Rameshbabu, R.; Ravi, P.; Sathish, M. Cauliflower-like CuS/ZnS nanocomposites decorated $g\text{-}C_3N_4$ nanosheets as noble metal-free photocatalyst for superior photocatalytic water splitting. *Chem. Eng. J.* **2019**, *360*, 1277–1286. [CrossRef]
18. Wu, Z.; Liu, X.; Yu, C.; Li, F.; Zhou, W.; Wei, L. Construct interesting CuS/TiO_2 architectures for effective removal of Cr(VI) in simulated wastewater via the strong synergistic adsorption and photocatalytic process. *Sci. Total Environ.* **2021**, *796*, 148941. [CrossRef]
19. Chandra, M.; Bhunia, K.; Pradhan, D. Controlled Synthesis of CuS/TiO_2 Heterostructured Nanocomposites for Enhanced Photocatalytic Hydrogen Generation through Water Splitting. *Inorg. Chem.* **2018**, *57*, 4524–4533. [CrossRef] [PubMed]
20. Lu, Y.Y.; Zhang, Y.Y.; Zhang, J.; Shi, Y.; Li, Z.; Feng, Z.C.; Li, C. In situ loading of CuS nanoflowers on rutile TiO_2 surface and their improved photocatalytic performance. *Appl. Surf. Sci.* **2016**, *370*, 312–319. [CrossRef]
21. Chen, Q.; Zhang, M.; Li, J.; Zhang, G.; Xin, Y.; Chai, C. Construction of immobilized 0D/1D heterostructure photocatalyst $Au/CuS/CdS/TiO_2$ NBs with enhanced photocatalytic activity towards moxifloxacin degradation. *Chem. Eng. J.* **2020**, *389*, 124476. [CrossRef]
22. He, H.Y. Facile synthesis of ultrafine CuS nanocrystalline/TiO_2: Fe nanotubes hybrids and their photocatalytic and Fenton-like photocatalytic activities in the dye degradation. *Microporous Mesoporous Mater.* **2016**, *227*, 31–38. [CrossRef]
23. Lee, H.; Kwak, B.S.; Park, N.-K.; Baek, J.-I.; Ryu, H.-J.; Kang, M. Assembly of a check-patterned CuS_x–TiO_2 film with an electron-rich pool and its application for the photoreduction of carbon dioxide to methane. *Appl. Surf. Sci.* **2017**, *393*, 385–396. [CrossRef]

24. Lin, H.; Li, L.; Zhao, M.; Huang, X.; Chen, X.; Li, G.; Yu, R. Synthesis of High-Quality Brookite TiO_2 Single-Crystalline Nanosheets with Specific Facets Exposed: Tuning Catalysts from Inert to Highly Reactive. *J. Am. Chem. Soc.* **2012**, *134*, 8328–8331. [CrossRef] [PubMed]
25. Wang, Y.; Lkhamjav, S.; Qiu, B.; Dong, C.; Dong, C.; Zhou, Y.; Shen, B.; Xing, M.; Zhang, J. A facile strategy to prepare Fe^{3+} modified brookite TiO_2 with high photocatalytic activity under ultraviolet light and visible light. *Res. Chem. Intermed.* **2017**, *43*, 2055–2066. [CrossRef]
26. Liu, L.; Zhao, H.; Andino, J.M.; Li, Y. Photocatalytic CO_2 Reduction with H_2O on TiO_2 Nanocrystals: Comparison of Anatase, Rutile, and Brookite Polymorphs and Exploration of Surface Chemistry. *ACS Catal.* **2012**, *2*, 1817–1828. [CrossRef]
27. Li, K.; Peng, T.; Ying, Z.; Song, S.; Zhang, J. Ag-loading on brookite TiO_2 quasi nanocubes with exposed {210} and {001} facets: Activity and selectivity of CO_2 photoreduction to CO/CH_4. *Appl. Catal. B* **2016**, *180*, 130–138. [CrossRef]
28. Li, K.; Peng, B.; Jin, J.; Zan, L.; Peng, T. Carbon nitride nanodots decorated brookite TiO_2 quasi nanocubes for enhanced activity and selectivity of visible-light-driven CO_2 reduction. *Appl. Catal. B* **2017**, *203*, 910–916. [CrossRef]
29. Jin, J.; Luo, J.; Zan, L.; Peng, T. One-Pot Synthesis of Cu-Nanocluster-Decorated Brookite TiO_2 Quasi-Nanocubes for Enhanced Activity and Selectivity of CO_2 Photoreduction to CH_4. *ChemPhysChem* **2017**, *18*, 3230–3239. [CrossRef]
30. Xiao, J.; Chen, S.; Jin, J.; Li, R.; Zhang, J.; Peng, T. Brookite TiO_2 Nanoparticles Decorated with Ag/MnO_x Dual Cocatalysts for Remarkably Boosted Photocatalytic Performance of the CO_2 Reduction Reaction. *Langmuir* **2021**, *37*, 12487–12500. [CrossRef]
31. Cho, K.M.; Kim, K.H.; Park, K.; Kim, C.; Kim, S.; Al-Saggaf, A.; Gereige, I.; Jung, H.-T. Amine-Functionalized Graphene/CdS Composite for Photocatalytic Reduction of CO_2. *ACS Catal.* **2017**, *7*, 7064–7069. [CrossRef]
32. Jin, L.; Shaaban, E.; Bamonte, S.; Cintron, D.; Shuster, S.; Zhang, L.; Li, G.; He, J. Surface Basicity of Metal@TiO_2 to Enhance Photocatalytic Efficiency for CO_2 Reduction. *ACS Appl. Mater. Interfaces* **2021**, *13*, 38595–38603. [CrossRef]
33. Yang, G.; Xiong, J.; Lu, M.; Wang, W.; Li, W.; Wen, Z.; Li, S.; Li, W.; Chen, R.; Cheng, G. Co-embedding oxygen vacancy and copper particles into titanium-based oxides (TiO_2, $BaTiO_2$, and $SrTiO_2$) nanoassembly for enhanced CO_2 photoreduction through surface/interface synergy. *J. Colloid Interface Sci.* **2022**, *624*, 348–361. [CrossRef] [PubMed]
34. Zhu, J.; Xiong, J.; Cheng, G.; Li, W.; Dou, S. Promoting solar-to-hydrogen evolution on Schottky interface with mesoporous TiO_2-Cu hybrid nanostructures. *J. Colloid Interface Sci.* **2019**, *545*, 116–127. [CrossRef] [PubMed]
35. Gan, Y.; Wei, Y.; Xiong, J.; Cheng, G. Impact of post-processing modes of precursor on adsorption and photocatalytic capability of mesoporous TiO_2 nanocrystallite aggregates towards ciprofloxacin removal. *Chem. Eng. J.* **2018**, *349*, 1–16. [CrossRef]
36. Wei, Y.; Cheng, G.; Xiong, J.; Zhu, J.; Gan, Y.; Zhang, M.; Li, Z.; Dou, S. Synergistic impact of cocatalysts and hole scavenger for promoted photocatalytic H_2 evolution in mesoporous TiO_2-NiS_x hybrid. *J. Energy Chem.* **2019**, *32*, 45–56. [CrossRef]
37. Zhu, Q.; Cao, Y.; Tao, Y.; Li, T.; Zhang, Y.; Shang, H.; Song, J.; Li, G. CO_2 reduction to formic acid via NH_2-C@Cu_2O photocatalyst in situ derived from amino modified Cu-MOF. *J. CO2 Util.* **2021**, *54*, 101781. [CrossRef]
38. Wang, S.; Zhao, X.; Muhammad Adeel Sharif, H.; Chen, Z.; Chen, Y.; Zhou, B.; Xiao, K.; Yang, B.; Duan, Q. Amine-CdS for exfoliating and distributing bulk MoO_2 for photocatalytic hydrogen evolution and Cr(VI) reduction. *Chem. Eng. J.* **2021**, *406*, 126849. [CrossRef]
39. Shao, Y.; Dou, Z.; Liang, X.; Zhang, X.; Ji, M.; Pang, M.; Wang, M.; Wang, X. $ZnIn_2S_4$ nanosheet growth on amine-functionalized SiO_2 for the photocatalytic reduction of CO_2. *Catal. Sci. Technol.* **2022**, *12*, 606–612. [CrossRef]
40. Liu, J.; Li, Y.; Ke, J.; Wang, S.; Wang, L.; Xiao, H. Black NiO-TiO_2 nanorods for solar photocatalysis: Recognition of electronic structure and reaction mechanism. *Appl. Catal. B* **2018**, *224*, 705–714. [CrossRef]
41. Torres, J.A.; da Cruz, J.C.; Nogueira, A.E.; da Silva, G.T.S.T.; de Oliveira, J.A.; Ribeiro, C. Role of Cu_0-TiO_2 interaction in catalyst stability in CO_2 photoreduction process. *J. Environ. Chem. Eng.* **2022**, *10*, 107291. [CrossRef]
42. Fu, J.; Cao, S.; Yu, J. Dual Z-scheme charge transfer in TiO_2–Ag–Cu_2O composite for enhanced photocatalytic hydrogen generation. *J. Mater.* **2015**, *1*, 124–133. [CrossRef]
43. Yuan, L.; Hung, S.-F.; Tang, Z.-R.; Chen, H.M.; Xiong, Y.; Xu, Y.-J. Dynamic Evolution of Atomically Dispersed Cu Species for CO_2 Photoreduction to Solar Fuels. *ACS Catal.* **2019**, *9*, 4824–4833. [CrossRef]
44. Zhang, F.; Li, Y.-H.; Qi, M.-Y.; Tang, Z.-R.; Xu, Y.-J. Boosting the activity and stability of Ag-Cu_2O/ZnO nanorods for photocatalytic CO_2 reduction. *Appl. Catal. B* **2020**, *268*, 118380. [CrossRef]
45. Li, Y.; Zhang, W.; Shen, X.; Peng, P.; Xiong, L.; Yu, Y. Octahedral Cu_2O-modified TiO_2 nanotube arrays for efficient photocatalytic reduction of CO_2. *Chin. J. Catal.* **2015**, *36*, 2229–2236. [CrossRef]
46. Liang, T.-Y.; Chan, S.-J.; Patra, A.S.; Hsieh, P.-L.; Chen, Y.-A.; Ma, H.-H.; Huang, M.H. Inactive Cu_2O Cubes Become Highly Photocatalytically Active with Ag_2S Deposition. *ACS Appl. Mater. Interfaces* **2021**, *13*, 11515–11523. [CrossRef] [PubMed]
47. Zhang, W.; Jiang, M.; Yang, S.; Hu, Y.; Mu, B.; Tie, Z.; Jin, Z. In-situ grown CuO_x nanowire forest on copper foam: A 3D hierarchical and freestanding electrocatalyst with enhanced carbonaceous product selectivity in CO_2 reduction. *Nano Res. Energy* **2022**, *1*, e9120033. [CrossRef]
48. Zhang, F.; Zhuang, H.-Q.; Zhang, W.; Yin, J.; Cao, F.-H.; Pan, Y.-X. Noble-metal-free CuS/CdS photocatalyst for efficient visible-light-driven photocatalytic H_2 production from water. *Catal. Today* **2019**, *330*, 203–208. [CrossRef]
49. Wang, Q.; Yun, G.; Bai, Y.; An, N.; Chen, Y.; Wang, R.; Lei, Z.; Shangguan, W. CuS, NiS as co-catalyst for enhanced photocatalytic hydrogen evolution over TiO_2. *Int. J. Hydrogen Energy* **2014**, *39*, 13421–13428. [CrossRef]
50. Zhang, L.J.; Xie, T.F.; Wang, D.J.; Li, S.; Wang, L.L.; Chen, L.P.; Lu, Y.C. Noble-metal-free CuS/CdS composites for photocatalytic H_2 evolution and its photogenerated charge transfer properties. *Int. J. Hydrogen Energy* **2013**, *38*, 11811–11817. [CrossRef]

51. Jiang, Y.; Zhang, M.; Xin, Y.; Chai, C.; Chen, Q. Construction of immobilized CuS/TiO_2 nanobelts heterojunction photocatalyst for photocatalytic degradation of enrofloxacin: Synthesis, characterization, influencing factors and mechanism insight. *J. Chem. Technol. Biotechnol.* **2019**, *94*, 2219–2228.
52. Wang, L.; Dong, Y.; Zhang, J.; Tao, F.; Xu, J. Construction of NiO/g-C_3N_4 p-n heterojunctions for enhanced photocatalytic CO_2 reduction. *J. Solid State Chem.* **2022**, *308*, 122878. [CrossRef]
53. Li, R.; Ma, H.; Shu, J.; Lian, Z.; Chen, N.; Ou, S.; Jin, R.; Li, S.; Yang, H. Surface engineering of copper sulfide-titania-graphitic carbon nitride ternary nanohybrid as an efficient visible-light photocatalyst for pollutant photodegradation. *J. Colloid Interface Sci.* **2021**, *604*, 198–207. [CrossRef] [PubMed]
54. Lu, Y.; Wu, D.; Qin, Y.; Xie, Y.; Ling, Y.; Ye, H.; Zhang, Y. Facile construction of BiOBr/CoAl-LDH heterojunctions with suppressed Z-axis growth for efficient photoreduction of CO_2. *Sep. Purif. Technol.* **2022**, *302*, 122090. [CrossRef]
55. Wang, L.; Wang, W.; Chen, Y.; Yao, L.; Zhao, X.; Shi, H.; Cao, M.; Liang, Y. Heterogeneous p–n Junction CdS/Cu_2O Nanorod Arrays: Synthesis and Superior Visible-Light-Driven Photoelectrochemical Performance for Hydrogen Evolution. *ACS Appl. Mater. Interfaces* **2018**, *10*, 11652–11662. [CrossRef]
56. Meng, F.; Li, J.; Cushing, S.K.; Zhi, M.; Wu, N. Solar Hydrogen Generation by Nanoscale p–n Junction of p-type Molybdenum Disulfide/n-type Nitrogen-Doped Reduced Graphene Oxide. *J. Am. Chem. Soc.* **2013**, *135*, 10286–10289. [CrossRef]
57. Aguirre, M.E.; Zhou, R.; Eugene, A.J.; Guzman, M.I.; Grela, M.A. Cu_2O/TiO_2 heterostructures for CO_2 reduction through a direct Z-scheme: Protecting Cu_2O from photocorrosion. *Appl. Catal. B* **2017**, *217*, 485–493. [CrossRef]
58. Yang, Q.; Qin, W.; Xie, Y.; Zong, K.; Guo, Y.; Song, Z.; Luo, G.; Raza, W.; Hussain, A.; Ling, Y.; et al. Constructing 2D/1D heterostructural BiOBr/CdS composites to promote CO_2 photoreduction. *Sep. Purif. Technol.* **2022**, *298*, 121603. [CrossRef]
59. Shafiq, I.; Hussain, M.; Rashid, R.; Shafique, S.; Akhter, P.; Yang, W.; Ahmed, A.; Nawaz, Z.; Park, Y.-K. Development of hierarchically porous $LaVO_4$ for efficient visible-light-driven photocatalytic desulfurization of diesel. *Chem. Eng. J.* **2021**, *420*, 130529. [CrossRef]
60. Cai, W.; Yu, X.; Cao, Y.; Hu, C.; Wang, Y.; Zhao, Y.; Bu, Y. Electron-coupled enhanced interfacial interaction of Ce-MOF/Bi_2MoO_6 heterostructure for boosted photoreduction CO_2. *J. Environ. Chem. Eng.* **2022**, *10*, 107461. [CrossRef]
61. Tang, Z.; Wang, C.; He, W.; Wei, Y.; Zhao, Z.; Liu, J. The Z-scheme g-C_3N_4/3DOM-WO_3 photocatalysts with enhanced activity for CO2 photoreduction into CO. *Chin. Chem. Lett.* **2022**, *33*, 939–942. [CrossRef]
62. Wu, X.; Wang, C.; Wei, Y.; Xiong, J.; Zhao, Y.; Zhao, Z.; Liu, J.; Li, J. Multifunctional photocatalysts of Pt-decorated 3DOM perovskite-type $SrTiO_3$ with enhanced CO_2 adsorption and photoelectron enrichment for selective CO_2 reduction with H_2O to CH_4. *J. Catal.* **2019**, *377*, 309–321. [CrossRef]
63. Xiong, J.; Zhang, M.; Lu, M.; Zhao, K.; Han, C.; Cheng, G.; Wen, Z. Achieving simultaneous Cu particles anchoring in meso-porous TiO_2 nanofabrication for enhancing photo-catalytic CO_2 reduction through rapid charge separation. *Chin. Chem. Lett.* **2022**, *33*, 1313–1316. [CrossRef]
64. Xiong, Z.; Lei, Z.; Kuang, C.-C.; Chen, X.; Gong, B.; Zhao, Y.; Zhang, J.; Zheng, C.; Wu, J.C.S. Selective photocatalytic reduction of CO_2 into CH_4 over Pt-Cu_2O TiO_2 nanocrystals: The interaction between Pt and Cu2O cocatalysts. *Appl. Catal. B* **2017**, *202*, 695–703. [CrossRef]
65. Tu, W.; Zhou, Y.; Li, H.; Li, P.; Zou, Z. Au@TiO_2 yolk–shell hollow spheres for plasmon-induced photocatalytic reduction of CO_2 to solar fuel via a local electromagnetic field. *Nanoscale* **2015**, *7*, 14232–14236. [CrossRef]
66. Kuai, L.; Zhou, Y.; Tu, W.; Li, P.; Li, H.; Xu, Q.; Tang, L.; Wang, X.; Xiao, M.; Zou, Z. Rational construction of a CdS/reduced graphene oxide/TiO_2 core–shell nanostructure as an all-solid-state Z-scheme system for CO_2 photoreduction into solar fuels. *RSC Adv.* **2015**, *5*, 88409–88413. [CrossRef]
67. Manzanares, M.; Fàbrega, C.; Oriol Ossó, J.; Vega, L.F.; Andreu, T.; Morante, J.R. Engineering the TiO_2 outermost layers using magnesium for carbon dioxide photoreduction. *Appl. Catal. B* **2014**, *150–151*, 57–62. [CrossRef]